

# Dependence of the Magnetic Energy of Solar Active Regions on the Twist Intensity of the Initial Flux Tubes

Shin TORIUMI<sup>1</sup> Takehiro MIYAGOSHI<sup>2</sup> Takaaki YOKOYAMA<sup>1</sup> Hiroaki ISOBE<sup>3</sup>  
and Kazunari SHIBATA<sup>4</sup>

<sup>1</sup>*Department of Earth and Planetary Science, University of Tokyo,  
Hongo, Bunkyo-ku, Tokyo 113-0033  
toriumi@eps.s.u-tokyo.ac.jp*

<sup>2</sup>*Japan Agency for Marine-Earth Science and Technology,  
Showa-machi, Kanazawa-ku, Yokohama 236-0001*

<sup>3</sup>*Unit of Synergetic Studies for Space, Kyoto University, Yamashina-ku, Kyoto 607-8471*

<sup>4</sup>*Kwasan and Hida Observatories, Kyoto University, Yamashina-ku, Kyoto 607-8471*

(Received ; accepted )

## Abstract

We present a series of numerical experiments that model the evolution of magnetic flux tubes with a different amount of initial twist. As a result of calculations, tightly twisted tubes reveal a rapid two-step emergence to the atmosphere with a slight slowdown at the surface, while weakly twisted tubes show a slow two-step emergence waiting longer the secondary instability to be triggered. This picture of the two-step emergence is highly consistent with recent observations. These tubes show multiple magnetic domes above the surface, indicating that the secondary emergence is caused by interchange mode of magnetic buoyancy instability. As for the weakest twist case, the tube exhibits an elongated photospheric structure and never rises into the corona. The formation of the photospheric structure is due to inward magnetic tension force of the azimuthal field component of the rising flux tube (i.e., tube's twist). When the twist is weak, azimuthal field cannot hold the tube's coherency, and the tube extends laterally at the subadiabatic surface. In addition, we newly find that the total magnetic energy measured above the surface depends on the initial twist. Strong twist tubes follow the initial relation between the twist and the magnetic energy, while weak twist tubes deviates from this relation, because these tubes store their magnetic energy in the photospheric structures.

**Key words:** magnetohydrodynamics: MHD, methods: numerical, Sun: corona, Sun: interior, Sun:photosphere

## 1. Introduction

Flux emergence is one of the key mechanisms in various solar activities. It is widely accepted that the emerging flux has a form of a twisted flux tube so as not to be collapsed by the convective motions during its ascent in the solar interior. Emerging flux transports magnetic energy and helicity from the convection zone to the atmosphere, which yields active regions including sunspots. Magnetic helicity in the corona stores free energy that can be released in the forms of flares and coronal mass ejections (CMEs) (e.g. Heyvaerts et al. 1977).

Many numerical experiments have revealed the dynamics of the flux emergence. Schüssler (1979) carried out two-dimensional magnetohydrodynamic (MHD) simulations to study the cross-sectional evolution of the emerging flux tube (see also Moreno-Insertis & Emonet 1996; Emonet & Moreno-Insertis 1998). Shibata et al. (1989) calculated the two-dimensional evolution of the undular mode of magnetic buoyancy instability (Parker instability: Parker 1966) to reproduce the formation of an  $\Omega$ -shaped coronal loops. Toriumi & Yokoyama (2010) and Toriumi & Yokoyama (2011) gave numerical studies of emerging fluxes from much deeper convection zone ( $\sim -20,000$  km) to the corona. The three-dimensionality also exerts an influence on emerging process of magnetic flux evolution. Matsumoto et al. (1993) produced the first three-dimensional work of the Parker instability using a magnetic flux sheet and a flux tube. Fan (2001) compared her numerical results of the twisted tube's emergence with observations of an active region.

In this paper, we perform three-dimensional simulations of the twisted emerging flux tube from the uppermost convection zone to the corona. Our aim is to study the effect of the initial twist on the emergence process. A series of parametric studies on the flux tube's twist was done by Murray et al. (2006). Our work is dedicated to further detailed analyses, especially focusing on the effect of the initial twist on the resulting tube's structure (photospheric lateral expansion and multiple magnetic domes) and on the consequent coronal magnetic energy.

For numerical experiments, we used the same conditions as those by Murray et al. (2006); we calculated ten cases of different twist parameters that cover their three runs. As a result of experiments, we found that the evolution depends on the initial twist. When the twist is strong enough, the evolution to the corona reveals two-step way, showing a deceleration and a lateral expansion near the solar surface, although the case with weaker twist spends more time waiting for the secondary emergence to occur (Magara 2001; Archontis et al. 2004; Murray et al. 2006). This picture of the two-step emergence is highly consistent with recent observations by Otsuji et al. (2010), especially its horizontally expanding speed and the rising speed. In addition to the confirmation of the results by Murray et al. (2006), it is also found that multiple magnetic domes are built and plasma accumulates in between the domes when the secondary emergence starts. At this moment, the direction of the field lines is almost perpendicular to the alignment of the domes, indicating that the second-step emergence is due to the interchange-mode instability.

If the initial twist is too weak, the tube extends widely near the surface and further evolution never takes place, because the magnetic tension force of the azimuthal component cannot hold the tube's coherency.

Also, we newly found that the total magnetic energy measured above the surface relies on the initial twist. In the strong twist regime, the resulting magnetic energy follows the initial relation between the twist and the magnetic energy. In the weak twist regime, however, the magnetic energy deviates from the initial rule, because the tube with weak twist stores magnetic energy around the photosphere.

The rest of the paper is organized as follows. In Section 2, we describe the numerical model. The simulation results are shown in Section 3. Summary and discussion are given in Section 4 and 5, respectively.

## 2. Numerical Setup

In numerical simulations, we solve nonlinear, time-dependent, compressible three-dimensional MHD equations. We take a rectangular computation box with three-dimensional Cartesian coordinates  $(x, y, z)$ , where the  $z$ -coordinate increases upward. The medium is assumed to be an inviscid perfect gas with a specific heat ratio  $\gamma = 5/3$ . The basic equations in vector form are as follows:

$$\frac{\partial \rho}{\partial t} + \nabla \cdot (\rho \mathbf{V}) = 0, \quad (1)$$

$$\frac{\partial}{\partial t}(\rho \mathbf{V}) + \nabla \cdot \left( \rho \mathbf{V} \mathbf{V} + p \mathbf{I} - \frac{\mathbf{B} \mathbf{B}}{4\pi} + \frac{\mathbf{B}^2}{8\pi} \mathbf{I} \right) - \rho \mathbf{g} = 0, \quad (2)$$

$$\frac{\partial \mathbf{B}}{\partial t} = \nabla \times (\mathbf{V} \times \mathbf{B}), \quad (3)$$

$$\frac{\partial}{\partial t} \left( \rho U + \frac{1}{2} \rho \mathbf{V}^2 + \frac{\mathbf{B}^2}{8\pi} \right) + \nabla \cdot \left[ \left( \rho U + p + \frac{1}{2} \rho \mathbf{V}^2 \right) \mathbf{V} + \frac{c}{4\pi} \mathbf{E} \times \mathbf{B} \right] - \rho \mathbf{g} \cdot \mathbf{V} = 0, \quad (4)$$

and

$$U = \frac{1}{\gamma - 1} \frac{p}{\rho}, \quad (5)$$

$$\mathbf{E} = -\frac{1}{c} \mathbf{V} \times \mathbf{B}, \quad (6)$$

$$p = \frac{k_{\text{B}}}{m} \rho T, \quad (7)$$

where  $U$  is the internal energy per unit mass,  $\mathbf{I}$  the unit tensor,  $k_{\text{B}}$  the Boltzmann constant,  $m$  the mean molecular mass, and  $\mathbf{g} = (0, 0, -g_0)$  the uniform gravitational acceleration. Other symbols have their usual meanings ( $\rho$  is for density,  $\mathbf{V}$  velocity vector,  $p$  pressure,  $\mathbf{B}$  magnetic field,  $c$  speed of light,  $\mathbf{E}$  electric field, and  $T$  temperature).

To make above equations dimensionless, we introduce normalizing units of length  $H_0$ , velocity  $C_{s0}$ , time  $\tau_0 \equiv H_0/C_{s0}$ , and density  $\rho_0$ , where  $H_0 = k_B T_0 / (m g_0)$  is the pressure scale height,  $C_{s0}$  the sound speed, and  $\rho_0$  the density at the photosphere, respectively. The gas pressure, temperature, magnetic field strength, and energy are normalized by the combinations of the units above, i.e.,  $p_0 = \rho_0 C_{s0}^2$ ,  $T_0 = m C_{s0}^2 / (\gamma k_B)$ ,  $B_0 = (\rho_0 C_{s0}^2)^{1/2}$ , and  $E_0 = \rho_0 C_{s0}^2 H_0^3$ , respectively. The gravity is given as  $g_0 = C_{s0}^2 / (\gamma H_0)$  by definition. For comparison of numerical results with observations, we use  $H_0 = 170$  km,  $C_{s0} = 6.8$  km s<sup>-1</sup>,  $\tau_0 = H_0 / C_{s0} = 25$  s, and  $\rho_0 = 1.4 \times 10^{-7}$  g cm<sup>-3</sup>, which are typical values for the solar photosphere. Then,  $p_0 = 6.3 \times 10^4$  dyn cm<sup>-2</sup>,  $T_0 = 5600$  K,  $B_0 = 250$  G, and  $E_0 = 3.1 \times 10^{26}$  erg.

The initial background stratification consists of three regions: an adiabatically stratified convective layer, a cool isothermal photosphere/chromosphere (afterward, we simply call it photosphere), and a hot isothermal corona. The photosphere and the corona are smoothly connected by the transition region. We take  $z/H_0 = 0$  to be the base height of the photosphere, and the starting height of the transition region and the corona are  $z_{\text{tr}}/H_0 = 10$  and  $z_{\text{cor}}/H_0 = 20$ , respectively. The initial temperature of the photosphere and the corona are  $T_{\text{ph}}/T_0 = 1$  and  $T_{\text{cor}}/T_0 = 150$ , respectively. The background temperature distribution in the transition region is given by

$$\frac{T_s(z)}{T_0} = \left( \frac{T_{\text{cor}}}{T_{\text{ph}}} \right)^{(z-z_{\text{tr}})/(z_{\text{cor}}-z_{\text{tr}})}, \quad (8)$$

and that of the convection zone being

$$\frac{T_s(z)}{T_0} = 1 - \frac{z}{T_0} \left| \frac{dT}{dz} \right|_{\text{ad}}, \quad (9)$$

where

$$\left| \frac{dT}{dz} \right|_{\text{ad}} = \frac{\gamma - 1}{\gamma} \frac{m g_0}{k_B} \quad (10)$$

is the adiabatic temperature gradient (subscript s is for surrounding distribution). The initial gas pressure and density profiles are defined by solving one-dimensional hydrostatic equation

$$\frac{d}{dz} p_s(z) + \rho_s(z) g_0 = 0 \quad (11)$$

and the equation of state (7) on the basis of the temperature distribution above.

The initial magnetic flux tube is embedded in the convection zone at  $z_{\text{tube}}/H_0 = -10$ . The longitudinal and azimuthal component of the flux tube are described as follows: for a radial distance from the axis  $r = [(y - y_{\text{tube}})^2 + (z - z_{\text{tube}})^2]^{1/2}$ ,

$$B_x(r) = B_{\text{tube}} \exp\left(-\frac{r^2}{R_{\text{tube}}^2}\right), \quad (12)$$

and

$$B_\phi(r) = q r B_x(r), \quad (13)$$

where  $(y_{\text{tube}}, z_{\text{tube}}) = (0, -10H_0)$  is the tube center,  $R_{\text{tube}}$  the radius,  $q$  the twist parameter, and  $B_{\text{tube}}$  the magnetic field strength at the axis. We take  $R_{\text{tube}}/H_0 = 2.5$  and  $B_{\text{tube}}/B_0 = 15$ , i.e., these parameters are almost the same as those of Murray et al. (2006). For pressure balance between the flux tube and the surrounding medium, the gas pressure inside the tube is obtained as  $p_i = p_s + \delta p_{\text{exc}}$ , where

$$\delta p_{\text{exc}} = \frac{B_x^2(r)}{8\pi} \left[ q^2 \left( \frac{R_{\text{tube}}^2}{2} - r^2 \right) - 1 \right]. \quad (14)$$

The density inside the tube is also defined as  $\rho_i = \rho_s + \delta \rho_{\text{exc}}$ , where

$$\delta \rho_{\text{exc}} = \frac{\delta p_{\text{exc}}}{p_s} \rho_s \exp\left(-\frac{x^2}{\lambda^2}\right), \quad (15)$$

and  $\lambda/H_0 = 20$ . That is, the flux tube is most buoyant at the middle of the tube ( $x/H_0 = 0$ ), and the buoyancy diminishes as  $|x|$  increases.

Here, we investigate ten parameters of  $q$ , which are  $qH_0 = 0.5, 0.4, 0.3, 0.25, 0.2, 0.175, 0.15, 0.125, 0.1, \text{ and } 0.05$ . The plasma beta ( $\beta \equiv 8\pi p/B^2$ ) at the tube center is  $\beta \sim 3$  at the initial state. The initial background stratification (gas pressure, density, and temperature) and the magnetic pressure along  $x/H_0 = y/H_0 = 0$  of the case  $qH_0 = 0.2$  are indicated in Figure 1.

The simulation domain is taken as  $(-120, -120, -20) \leq (x/H_0, y/H_0, z/H_0) \leq (120, 120, 150)$ , resolved by  $256 \times 256 \times 256$  grids. The grid spacings for  $x$ ,  $y$ , and  $z$  directions are  $\Delta x/H_0 = \Delta y/H_0 = 0.5$  for  $(-40, -40) \leq (x/H_0, y/H_0) \leq (40, 40)$ , and  $\Delta z/H_0 = 0.2$  for  $-20 \leq z/H_0 \leq 20$ , respectively. Outside this range, the mesh sizes gradually increase. We assume periodic boundaries for horizontal directions and symmetric for vertical. A wave-damping region is attached near the top boundary. We use the modified Lax-Wendroff scheme version of the CANS (Coordinated Astronomical Numerical Software) code (see Toriumi & Yokoyama 2010).

### 3. Results

#### 3.1. Overview of the Results

Figure 2 shows the time evolution of the flux tube with the twist  $qH_0 = 0.2$ . In this Figure, we plot the logarithmic field strength  $\log(|B|/B_0)$  and the photospheric magnetogram  $B_z/B_0$ . In each panel, the region  $x/H_0 \leq 0$  and  $y/H_0 \geq 0$  is shown. Initially, the flux tube is embedded at  $z_{\text{tube}}/H_0 = -10$ , and is slightly buoyant around the tube center  $-20 < x/H_0 < 20$ . The tube rises through the convection zone by magnetic buoyancy, and reaches the surface at  $t/\tau_0 = 20$  (Figure 2(b)), while the outskirts of the rising portion ( $x/H_0 \sim -20$ ) begins to sink, because the fluid is drained along the field lines from the apex of the rising tube. Due to the isothermal (i.e., strongly-subadiabatic) photosphere, the tube is decelerated and expands laterally near the surface to make a ‘‘photospheric tongue’’ (Figure 2(c)). That is, the convectively stable photosphere inhibits an upward motion of the fluid, and thus, the mag-

netic field cannot penetrate the photosphere only to escape in the horizontal direction. (It should be noted that the term “tongue” here is different from that used in Li et al. (2007) and Archontis & Hood (2010). The horizontal extension of the magnetic field is also observed in a recent radiative MHD calculation by Cheung et al. (2010). The lateral expansion speed is  $|V_y| \sim 0.4C_{s0} = 2.7 \text{ km s}^{-1}$ , i.e., a fraction of the photospheric sound speed. At this moment, the photospheric magnetogram shows a north-south ( $y$ -directional) magnetic distribution, and the total field strength is  $|B| \sim 2B_0 = 500 \text{ G}$  and plasma beta is  $\beta \equiv p/p_{\text{mag}} \sim 2$  around the photosphere.

As the magnetic pressure gradient enhances, the second-step emergence takes place. In Figure 2(d), multiple expansions are observed: the rise velocity is about  $(0.3 - 0.5)C_{s0} = 2.0 - 3.4 \text{ km s}^{-1}$ . This multi-dome structure is more noticeable in a weaker twist case. Figure 3(a) shows the magnetic field structure of the case  $qH_0 = 0.15$  at  $t/\tau_0 = 80$ . The corresponding density structure and velocity vectors in the  $y/H_0 = 0$  plane, and the field lines are indicated in Figure 3(b). From these figures, one can see four magnetic domes are built and the fluid is accumulated between the domes. In this region, the field lines are generally directed in the  $y$ -direction. Therefore, this situation can be explained as a consequence of the interchange mode of the magnetic buoyancy instability, i.e., the wavenumber vector is perpendicular to the field lines.

As time goes on, the flux tube expands both vertically and horizontally, while the photospheric tongue also continues to expand laterally (Figure 2(e)). Finally, the flux tube makes a single dome of the height  $z/H_0 \sim 60$  on the pancake-like structure at the surface (Figure 2(f)). At the same time, the sunk part approaches the bottom of the simulation domain ( $z/H_0 \sim -20$ ).

Overall evolution described above is similar to the observation by Otsuji et al. (2010). They found the lateral expansion with the speed of  $2.9 \text{ km s}^{-1}$  at the surface before further evolution occurred, which is consistent with our results of  $|V_y| = 2.7 \text{ km s}^{-1}$ . The gradual rise speed of the secondary emergence was observed to be  $2.1 \text{ km s}^{-1}$ , which is also consistent with our results of  $2.0 - 3.4 \text{ km s}^{-1}$ .

### 3.2. Parameter Study on the Twist Strength

Figure 4 shows the height-time relation of the top of the tube for various twist cases. Here, in this figure, we plot the height at the highest portion of the emerging flux tube ( $z_{\text{apex}}/H_0$ ). The evolutions are found to depend on the initial twist, and each line distributes in a continuous fashion. It can be seen from this figure that almost all the tubes ( $0.5 \geq qH_0 \geq 0.1$ ) show the two-step emergence to the corona. Although the rise times within the convection zone are similar to each other, tubes with weaker twists spend more time in the surface waiting for the second-step emergence to be triggered. The tube with  $qH_0 = 0.1$  shows only a slight emergence in the atmosphere ( $z/H_0 \lesssim 20$ ). As for the weakest twist case with  $qH_0 = 0.05$ , further evolution never takes place within the elapse calculated (failed emergence). These results are

consistent with those of Magara (2001), Murray et al. (2006), and Toriumi & Yokoyama (2011).

Cross-sections at  $x/H_0 = 0$  plane of eight out of ten flux tubes are shown in Figure 5. These tubes are those who reach  $z/H_0 = 40$ , and each figure shows the arrival at that height. As the initial twist  $qH_0$  becomes smaller, the lateral expansion at the surface (tongue-like structure around  $z/H_0 \sim 0$ ) is increasingly remarkable, because the more intense initial twist of the magnetic flux tube yields the stronger azimuthal magnetic tension force, and thus keeps the tube coherent. Therefore, the coronal field intensity also reduces with decreasing  $qH_0$ , and the coronal structure with a weaker twist is more fragmented compared to the stronger twist cases.

### 3.3. Comparison of the Magnetic Field Structure at the Surface

In this subsection, we compare the magnetic field structures of the different emergence cases to study the horizontal expansion and the mechanism of the second-step evolution at the solar surface. Figure 6 shows (*top*) the cross-sectional configuration of the flux tubes at  $x/H_0 = 0$  with velocity vectors, (*middle*) the horizontal components of forces along the horizontal axis  $x/H_0 = z/H_0 = 0$ , and (*bottom*) the vertical components of forces along the vertical axis  $x/H_0 = y/H_0 = 0$  for cases with  $qH_0 = 0.4$  (rapid emergence), 0.15 (slow emergence), and 0.05 (failed emergence) at the time  $t/\tau_0 = 40$ .

As can be seen from the top figures, the second-step evolution has already begun at this time for the case with  $qH_0 = 0.4$ , while the vertical expansion cannot be seen in  $qH_0 = 0.05$  case. It should be noted that the downflow in the uppermost areas in Figures 6(b) and (c) is a reflected wave from the top boundary. Horizontally, for a strongest twist case (Figure 6(d)), an inward magnetic tension force is dominant, and thus the inward total force keeps the tube from a lateral fragmentation. As the twist decreases, the magnetic tension reduces so that the total force is outward in a wider range for  $qH_0 = 0.05$  (Figure 6(f)), resulting in the tube's fragmentation and the further expansion never to occur. As for vertical forces, magnetic pressure gradient is principal at front of the tube (Figure 6(g):  $3 < z/H_0 < 9$ ). However, the total force is about zero within this area. That is, the second-step expansion is caused by the tube's magnetic pressure, while the tube is almost in a hydrostatic equilibrium with surrounding materials. For a weak twist case (Figure 6(i)), the magnetic pressure gradient is much less effective. Therefore, further rise cannot occur.

### 3.4. Undulating Configuration of the Photospheric Field Lines

Figure 7 shows the surface magnetogram  $B_z/B_0$  and the field lines above the surface for the medium twist case ( $qH_0 = 0.15$ ) at the time  $t/\tau_0 = 125$ , namely, in the later phase. We confirm that some undulating field lines connect magnetic patches at the surface, and that, as time goes on, they gradually rise into the corona by forming longer fields. At this time, both near-surface undulating fields and coronal fields are directed almost parallel to the axis of the original flux tube, which is in contrast to the perpendicular fields observed in the earlier phase

of the emergence (see Figure 3(b)). This result is reminiscent of the “sea-serpent” field lines and the resistive emergence by Pariat et al. (2004). Undulating photospheric fields of a weakly twisted tube are also found by Archontis & Hood (2010). We will discuss this again in Section 5.

### 3.5. Magnetic Energy in the Atmosphere and the Initial Tube’s Twist

Figure 8 shows the initial twist  $qH_0$  and the total magnetic energy measured above the solar surface  $E_{\text{mag}}/E_0$  when each tube arrives at  $z/H_0 = 40$  (see Figure 5). The magnetic energy above the surface is defined as:

$$E_{\text{mag}} = \int_{z>0} \frac{B^2}{8\pi} dV. \quad (16)$$

When the initial twist is large ( $qH_0 \geq 0.2$ ), the magnetic energy  $E_{\text{mag}}$  is found to obey a  $q^2$  law. From the field configuration (12) and (13), the initial magnetic energy per unit volume can be calculated as

$$\frac{B^2}{8\pi} = (q^2 r^2 + 1) \frac{B_{\text{tube}}^2}{8\pi} \exp\left(-\frac{2r^2}{R_{\text{tube}}^2}\right), \quad (17)$$

that is, the initial tube’s magnetic energy depends on  $q^2$ . When the twist is strong, the azimuthal magnetic tension force is more effective and the lateral expansion around the photosphere is less efficient that the initial magnetic energy is directly transported into the atmosphere above the surface. As a result of this regime, the observed magnetic energy within the atmosphere relies on a  $q^2$  function.

Contrary to this, when the initial twist is weak ( $qH_0 \leq 0.2$ ), the consequent magnetic energy deviates from the  $q^2$  line and is negatively-correlated with the initial twist. It is speculated that, for these tubes with weaker twists, it takes a longer time to reach  $z/H_0 = 40$  from the surface. It is because the photospheric field needs more time to satisfy the condition for the second-step emergence (i.e. Acheson 1979), for the weak azimuthal field causes the tube to expand horizontally around the surface. Since the magnetic energy is continuously transported from below and the horizontal expanding velocity is almost the same for  $qH_0 \leq 0.2$  cases ( $V_y/C_{s0} \sim 0.1$ ), the magnetic energy of the photospheric tongue is expected to depend on the time lag between the tube’s arrival at the photosphere and at  $z/H_0 = 40$ .

It can be concluded that the magnetic energy in the atmosphere correlates critically with the initial twist. In the strong twist regime, the energy-twist relation follows the initial  $q^2$  rule, because the tightly twisted tube does not exhibit a significant expansion near the photosphere. As for the weak twist cases, they depend on the time lag between reaching the photosphere and the corona. It is because the weaker twist tube takes more time to rise further, and, therefore, more magnetic energy is stored in the photospheric tongue.

## 4. Summary

In this paper, we carried out three-dimensional MHD simulations to investigate the effect of the initial twist on the flux tube evolution. Here, we summarize the results:

- Initially, the flux tube rises through the convection zone due to its magnetic buoyancy. Reaching the surface, the tube expands laterally to make a “photospheric tongue.” The secondary emergence occurs after sufficient flux accumulates within the photosphere. Due to the interchange mode instability, the tube builds multiple domes above the surface, between which the fluids piles up. Finally, the flux tube arrives at  $z/H_0 \sim 60$  as a single dome. The overall emergence is consistent with the recent observations (e.g. Otsuji et al. 2010).
- We run ten twist cases to investigate the effect of the initial twist. Nine out of ten reach the coronal height ( $z/H_0 \geq 20$ ) showing two-step emergence, while the weakest twist case fails to rise further above the surface ( $qH_0 = 0.05$ ). In the two-step emergence regime, the rise time becomes shorter with increasing initial twist, which is consistent with the previous calculations by Murray et al. (2006). The photospheric tongue is more noticeable in weaker twist case.
- We study the force components at the solar surface for different twist cases at the time  $t/\tau_0 = 40$ . The stronger the initial twist is, the larger the inward magnetic tension is, resulting the tube keeps its coherency. In the weak twist case, the magnetic tension is much less effective, causing the tube distorted. At the same time, the strong twist tube rises further into the atmosphere mainly by the magnetic pressure gradient.
- We found that the photospheric fields of the middle twist case ( $qH_0 = 0.15$ ) undulate in the later phase of the emergence. The field lines gradually rise into the corona as longer loops. The photospheric and coronal fields are almost parallel to the axis of the initial flux tube. These features remind us of the resistive emergence model by Pariat et al. (2004).
- We measure the magnetic energy  $E_{\text{mag}}$  above the surface. The energy plot follows the initial  $q^2$  law when the twist is strong ( $qH_0 \geq 0.2$ ), while, for weaker twist cases ( $qH_0 \leq 0.2$ ), the energy depends on the time difference between reaching the surface and the corona. That is, weakly twisted tube takes more time for magnetic flux to accumulate near the surface and the secondary instability to be triggered.

## 5. Discussion

In Section 3, we showed the time-evolution of the twisted flux tube. When the second-step emergence starts, multiple domes are observed above the surface and fluid is trapped between the expanding magnetic structures (see Figure 3). At this time, field lines are directed perpendicular to the alignment of the magnetic domes. For middle twist tube, we also found undulating fields near the surface, emerging into the corona (see Figure 7). In this section, we

discuss these features in connection with future observations.

### 5.1. *Twist Intensity and the Interchange Instability*

In Section 3.1, we saw that, as the twist decreases, the interchange mode instability becomes more noticeable. However, this is contrary to the expectation that the azimuthal field should be less pronounced in a weaker twist case. It may be because, in a weak twist case, the tube extends laterally near the photosphere and thus the twist increases. As the tube develops the interchange instability, field lines perpendicular to the alignment of the magnetic domes become more pronounced (see Sections 3.2 and 3.3).

### 5.2. *Twist of the Actual Flux Tube in the Sun*

Multiple magnetic structures and the density accumulation between them are also found in previous observations and calculations. Pariat et al. (2004) found that photospheric fields are undulating at its earlier phase of the flux emergence event, and proposed a resistive emergence model that undulating multiple loops reconnect with each other to make larger coronal fields. Isobe et al. (2007) carried out two-dimensional MHD simulation to study the evolution of the serpentine magnetic loops (resistive emergence model), finding that density accumulates in between the magnetic loops; their elongated vertical plasma structures are similar to our results (for three-dimensional study, see Archontis & Hood (2009)). However, in our model, field lines are directed almost perpendicular to the alignment of the domes, which is against the observations of the undular field lines (e.g. Pariat et al. 2004). The direction of the field lines are the consequence of the initial tube's twist. Therefore, the difference between the present calculations and the observations indicates that the actual twist of the flux tube beneath the surface may be much weaker than those assumed in our models (e.g.  $qH_0 = 0.15$  for Figure 3).

On the other hand, flux tube with insufficient twist was found to fail to rise through the convection zone (Moreno-Insertis & Emonet 1996; Emonet & Moreno-Insertis 1998; Toriumi & Yokoyama 2011). It is because the weak azimuthal field of the flux tube cannot hold its coherency during its ascent within the solar interior. Therefore, one of the important problems to be solved is the emergence of the flux tube with much weaker twist ( $qH_0 \leq 0.1$ ).

We also found that the medium twist tube ( $qH_0 = 0.15$ ) reveals the undulating fields at the surface, which gradually rise into the upper atmosphere as longer coronal loops (Section 7). These fields are directed parallel to the main axis of the initial flux tube. This picture seems well accorded with the resistive emergence model. However, it is in the later phase that this undulatory evolution is observed, and, in the earlier phase, the field lines are perpendicular to the original tube's axis (see Figure 3). Therefore, the reproduction of the undulating fields parallel to the original axis (Pariat et al. 2004) is not achieved.

### 5.3. Formation of Undulating Photospheric Fields

Recently, Cheung et al. (2010) have conducted a radiative MHD simulation of the formation of an active region. They showed that the rising flux tube flattens to make a pancake-like structure near the surface, and that the convective flows create serpentine field lines.

In the present study, which does not include the convection, we also found the sideway expansion of the rising field at the photosphere (tongue) and the undulation of the photospheric fields in the later phase of the emergence of the weaker twist tube. These features are also confirmed by Archontis & Hood (2010); their simulations do not take account of the convection effects, either. Therefore, we can see that other mechanisms, apart from the convection, could also explain the formation of serpentine fields at the photosphere.

### 5.4. For Future Observations

In this paper, we found some aspects of the flux emergence event. One is the photospheric tongue, i.e., the magnetic structure extending horizontally around the surface just before further evolution takes place. Temporally- and spacially-resolved spectroscopic observations of the earlier phase of the flux emergence are required to study this magnetic extension at the photosphere.

At the same time, we found that the initial twist of  $qH_0 \sim 0.1$  at  $-1700$  km is too strong to match the observations (as mentioned above in Section 5.2). Local and global helioseismology are needed to reveal the flux emergence (especially on the twist evolution) within the convection zone. The key issue is how weakly twisted flux tubes manage to rise through the solar interior.

Numerical computations were carried out on NEC SX-9 at the Center for Computational Astrophysics, CfCA, of the National Astronomical Observatory of Japan, and on M System (Fujitsu FX1) of JAXA Supercomputer System. The page charge of this paper is partly supported by CfCA. S. T. and T. Y. thank Dr. Y. Fan of the High Altitude Observatory, the National Center for Atmospheric Research. We thank the referee for helpful suggestions for improvements of this paper.

## References

- Acheson, D. J. 1979, *Sol. Phys.*, 62 23  
Archontis, V., Moreno-Insertis, F., Galsgaard, K., Hood, A., & O’Shea, E. 2004, *A&A*, 426, 1047  
Archontis, V., & Hood, A. W. 2010, *A&A*, 508, 1469  
Archontis, V., & Hood, A. W. 2010, *A&A*, 514, 56  
Cheung, M. C. M., Rempel, M., Title, A. M., & Schüssler, M. 2010, *ApJ*, 720, 233  
Emonet, T., & Moreno-Insertis, F. 1998, *ApJ*, 492, 804  
Fan, Y. 2001, *ApJL*, 554, L111  
Heyvaerts, J., Priest, E. R., & Rust, D. M. 1977, *ApJ*, 216, 123

Isobe, H., Tripathi, D., & Archontis, V. 2007, ApJL, 657, L531  
Li, H., Schmieder, B., Song, M. T., & Bommier, V. 2007, A&A, 475, 1081  
Magara, T. 2001, ApJ, 549, 608  
Matsumoto, R., Tajima, T., Shibata, K., & Kaisig, M. 1993, ApJ, 414, 357  
Moreno-Insertis, F., & Emonet, T. 1996, ApJ, 472, L53  
Murray, M. J., Hood, A. W., Moreno-Insertis, F., Galsgaard, K., & Archontis, V. 2006, A&A, 460, 909  
Otsuji, K. et al. 2010, PASJ, 62, 893  
Pariat, E. Aulanier, G., Schmieder, B., Georgoulis, M. K., Rust, D. M., & Bernasconi, P. N. 2004, ApJ, 614, 1099  
Parker, E. N. 1966, ApJ, 145, 811  
Schüssler, M. 1979, A&A, 71, 79  
Shibata, K., Tajima, T., Steinolfson, R. S., & Matsumoto, R. 1989, ApJ, 345, 584  
Toriumi, S., & Yokoyama, T. 2010, ApJ, 714, 505  
Toriumi, S., & Yokoyama, T. 2011, ApJ, submitted

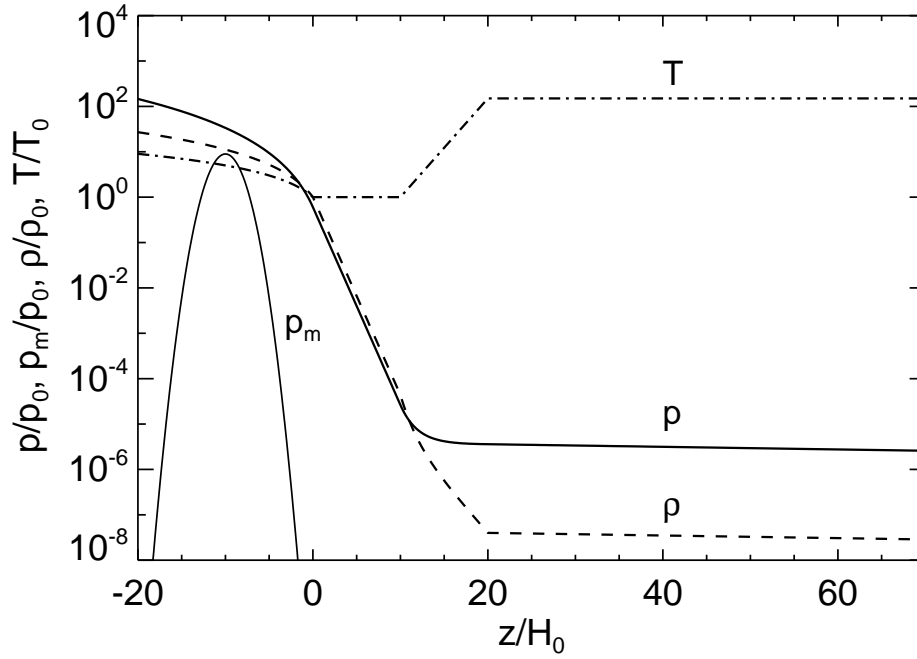


**Fig. 1.** One-dimensional ( $z$ -)distributions of the initial background density (thick solid line), pressure (dotted line), and temperature (dashed line). The magnetic pressure  $p_m = B^2/(8\pi)$  of the tube  $qH_0 = 0.2$  along the vertical axis  $x/H_0 = y/H_0 = 0$  is overplotted with a thin solid line.

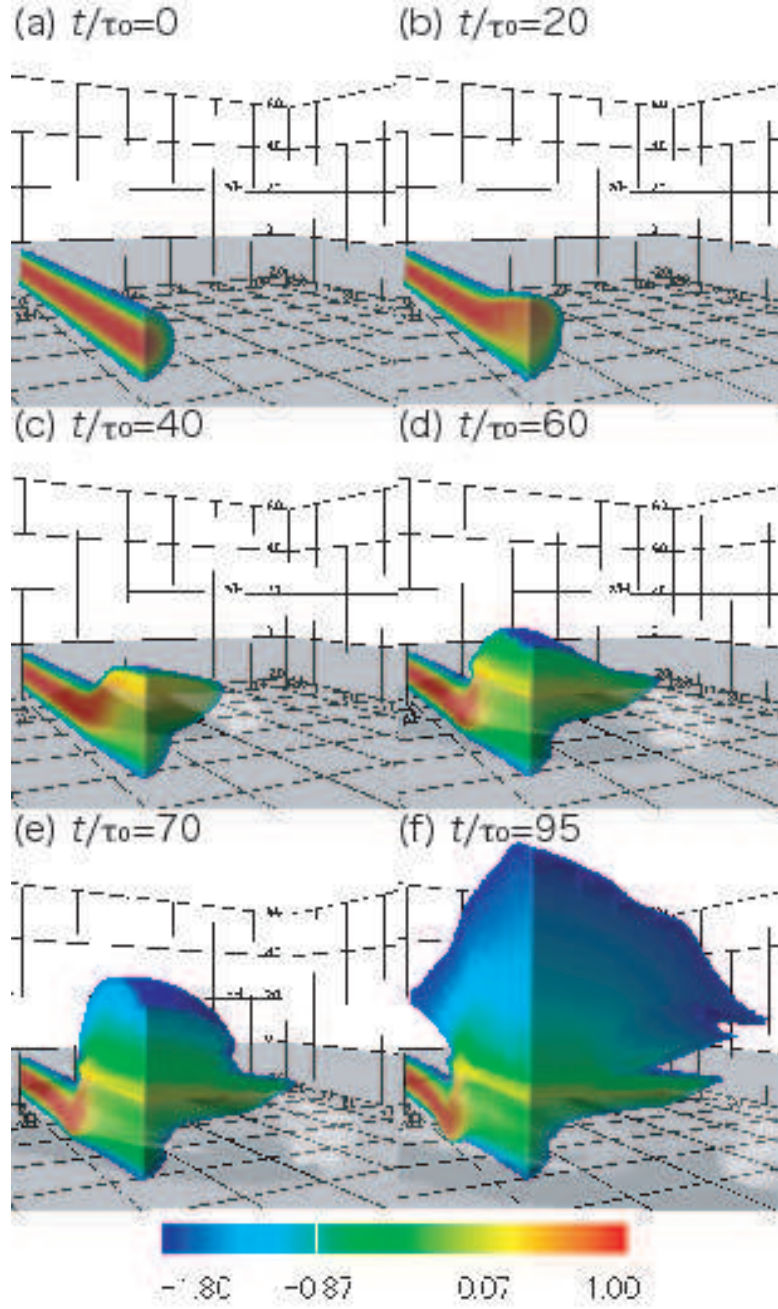


**Fig. 2.** Time evolution of the flux tube with the twist  $qH_0 = 0.2$ . Logarithmic field strength  $\log(|B|/B_0)$  and photospheric magnetogram  $B_z/B_0$  are plotted. In each panel, the region  $x/H_0 \leq 0$  and  $y/H_0 \geq 0$  is shown. This figure is also available as an avi animation in the electronic edition.

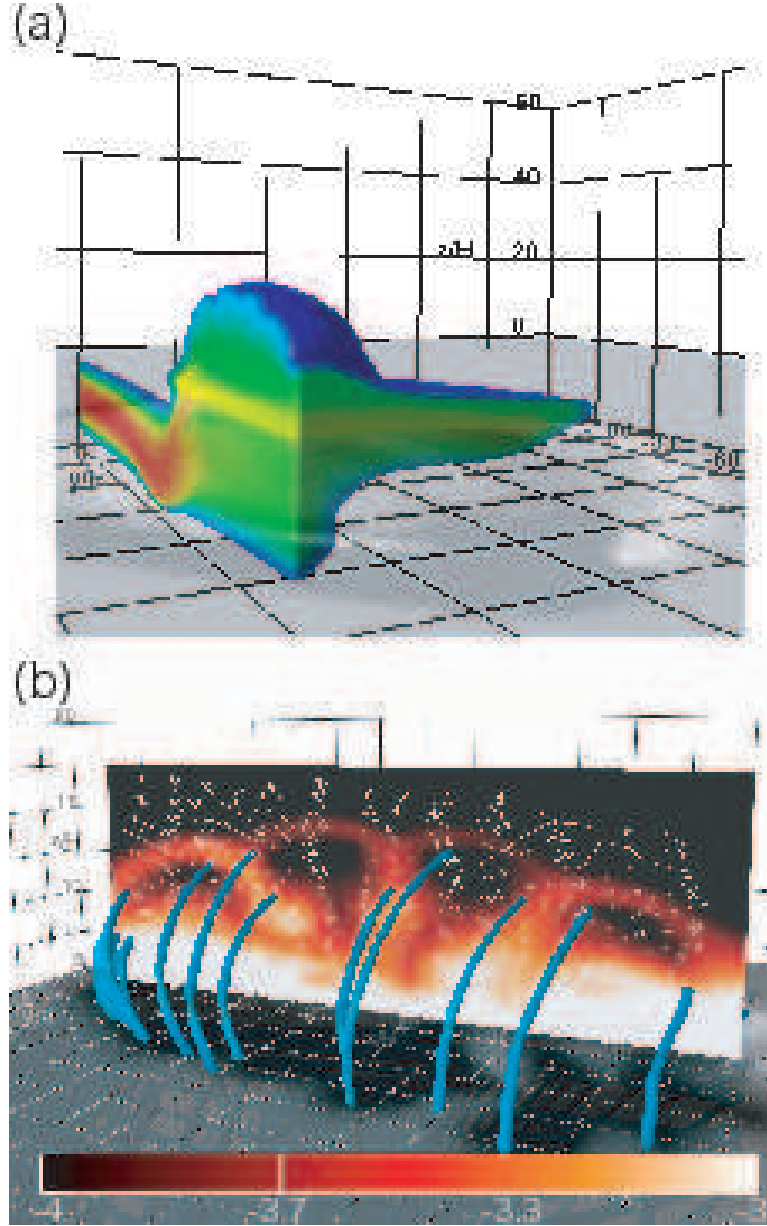


**Fig. 3.** The flux tube with  $qH_0 = 0.15$  at the time  $t/\tau_0 = 80$ . (a) Magnetic field structure  $\log(|B|/B_0)$  and photospheric magnetogram  $B_z/B_0$ . Plotted colors are the same as those of Figure 2. (b) The corresponding logarithmic density profile  $\log(\rho/\rho_0)$  at  $y/H_0 = 0$  plane ( $-40 \leq x/H_0 \leq -5$  and  $5 \leq z/H_0 \leq 17.5$ ) with velocity vectors (white arrows), magnetogram at  $z/H_0 = 5$ , and field lines (blue lines) are shown.

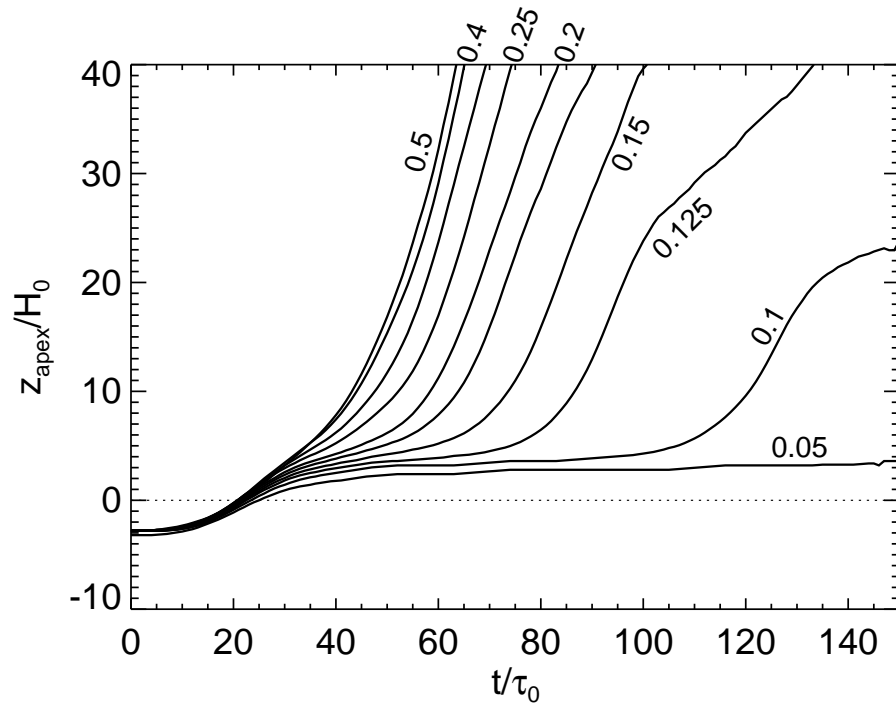


**Fig. 4.** Height-time relations for various twist cases. From left to right, each line shows the evolution of  $qH_0 = 0.5, 0.4, 0.3, 0.25, 0.2, 0.175, 0.15, 0.125, 0.1,$  and  $0.05$ . It takes more time to rise into the corona as the twist strength decreases.

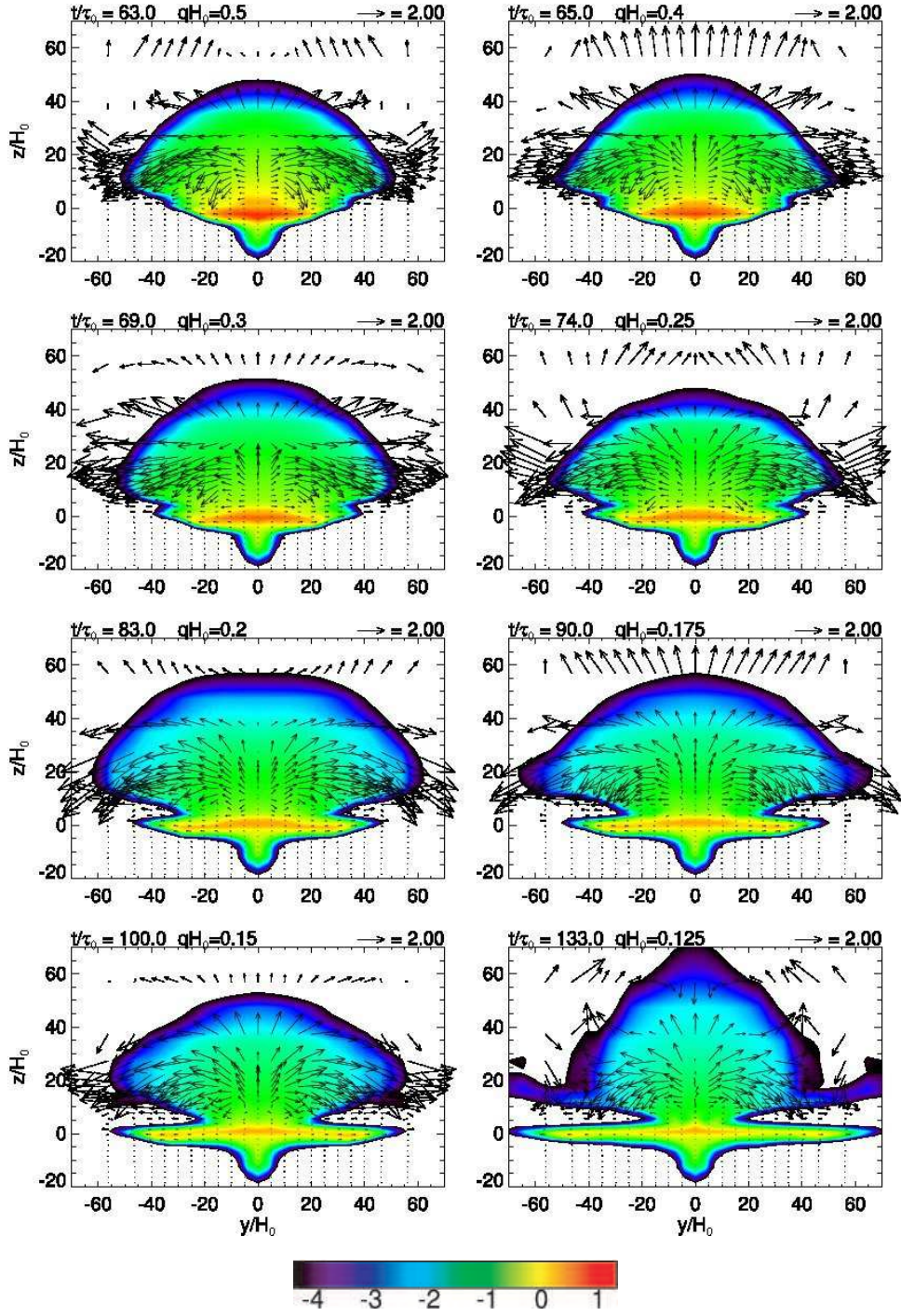
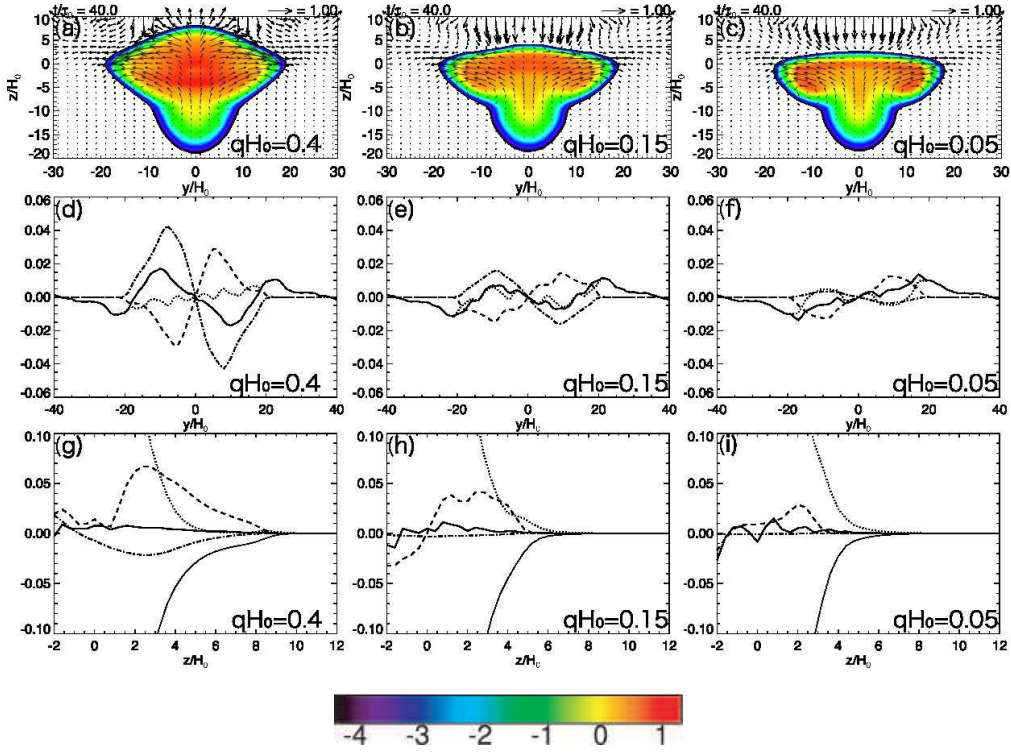
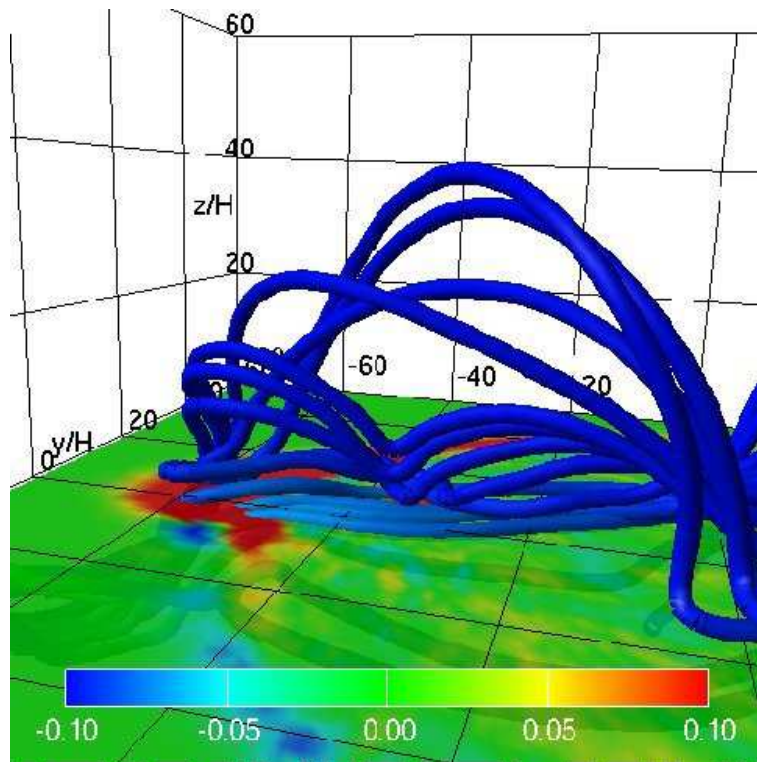


Fig. 5. Cross-sections at  $x/H_0 = 0$  plane of eight out of ten flux tubes that reach  $z/H_0 = 40$ . Each figure shows the logarithmic field strength  $\log(|B|/B_0)$  when the tube reaches that height.



**Fig. 6.** (Top) Cross-sectional configuration of the flux tubes at  $x/H_0 = 0$  with velocity vectors, (middle) horizontal components of each force along the horizontal axis  $x/H_0 = z/H_0 = 0$ , and (bottom) vertical components of forces along the vertical axis  $x/H_0 = y/H_0 = 0$  for cases with  $qH_0 = 0.4$  (rapid emergence), 0.15 (slow), and 0.05 (failed) at the time  $t/\tau_0 = 40$ . Plotted lines are the total force (thick solid line), gas pressure gradient (dotted), magnetic pressure gradient (dashed), magnetic tension (dash-dotted), and gravity (thin solid), respectively.



**Fig. 7.** Surface magnetogram  $B_z/B_0$  (color contour) and the field lines (blue lines) for the middle twist case ( $qH_0 = 0.15$ ) at the time  $t/\tau_0 = 125$  are shown. Note that some field lines undulate near the surface and gradually rise into the corona as longer loops.

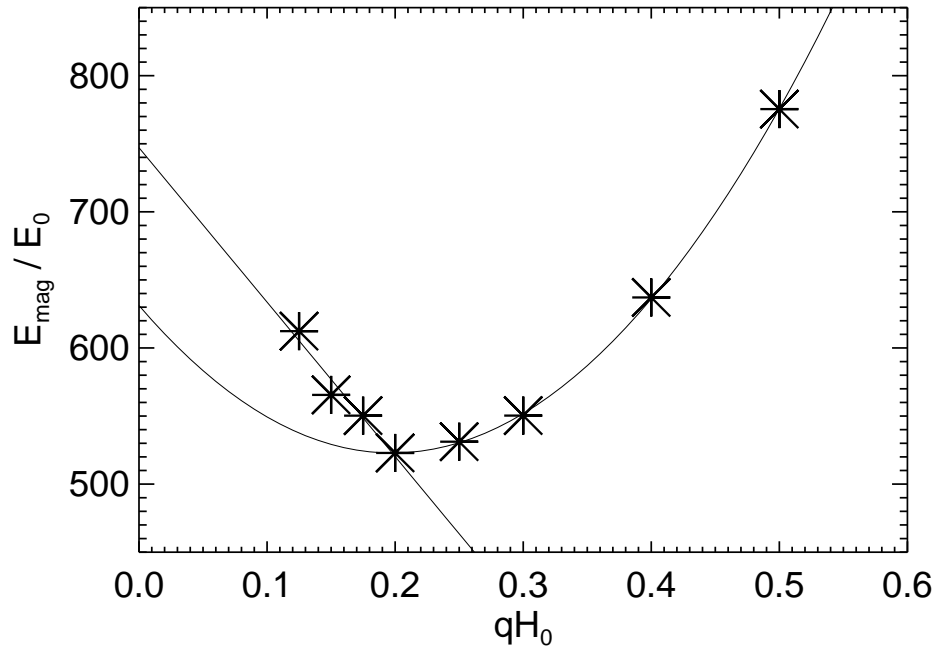


**Fig. 8.** Total magnetic energy above the surface  $E_{\text{mag}} = \int_{z>0} B^2 / (8\pi) dV$  versus the initial twist  $q$ , measured at the time when each tube reaches  $z/H_0 = 40$ . Quadratic and linear lines are overlotted with solid lines.